Multipath Exploitation in Through-the-Wall Radar Imaging using Sparse Reconstruction

Michael Leigsnering, *Student Member, IEEE,* Fauzia Ahmad, *Senior Member, IEEE,*

Moeness G. Amin, *Fellow, IEEE,* and Abdelhak M. Zoubir, *Fellow, IEEE*

Abstract

Multipath exploitation and compressive sensing (CS) have both been applied independently to through-the-wall radar imaging. Fast and efficient data acquisition is desired in scenarios where multipath effects cannot be neglected. Hence, we combine the two methods to achieve good image reconstruction in multipath environments from few spatial and frequency measurements. Ghost targets appear in the scene primarily due to specular reflections from interior walls and multiple reflections within the front wall. Assuming knowledge of the room geometry, we can invert the multipath model and eliminate ghosts by means of CS. We develop effective methods for the reconstruction of stationary scenes which employ a group sparse CS approach. Additionally, we separate the target and wall contributions to the image by a sparse reconstruction approach joining wall and target models which allows suppression of the ghosts and increased signal-to-clutter ratio at the target locations. Effectiveness of the proposed approach is demonstrated using both simulated and real data.

Index Terms

Compressive sensing (CS), sparse reconstruction, multipath exploitation, through-the-wall radar imaging (TWRI), wall clutter.

I. INTRODUCTION

Imaging through building walls using radar has drawn much attention due to its numerous civil and military applications [1]–[4]. Through-the-wall radar imaging (TWRI) has the potential of revealing stationary and moving targets behind an opaque obstacle. Ongoing research in this area aims at obtaining clean and highly resolved images of a scene of interest.

One major challenge in TWRI is the clutter caused by reflections from exterior and interior walls. Another challenge is the multipath stemming from multiple reflections of electromagnetic (EM) waves off the targets in

conjunction with the walls. In a multi-antenna radar system or synthetic aperture radar (SAR), multipath delayed returns may result in the power being focused at pixels different than those corresponding to the target. This gives rise to ghosts, which can be confused with the real targets inside buildings [5]. Hence, ghosts need to be addressed in order to provide proper representation of the ground truth. The front wall facing the radar poses two additional problems, apart from its strong reflections and significant radar returns. First, the transmitted power through the wall may not be sufficient to reach the targets and reflect back to the radar, leading to missed detections. Second, the multiple reflections within the wall result in wall residuals along the range dimension. These wall reverberations can be stronger than target reflections, leading to its masking and undetectability, especially for targets close to the wall. The first wall problem can only be addressed by emitting more power, whereas the second problem can be successfully tackled through re-focusing and wall mitigation techniques [6]–[9].

In this paper, we consider the problem of multipath and wall reverberations in view of the requirements of fast data acquisition and reduced measurements. High-resolution imaging demands large aperture and bandwidth, which result in a large amount of data to be acquired, stored, and processed. To address this problem in the context of TWRI, compressive sensing (CS) was first applied by Yoon and Amin [10], providing an efficient way of data acquisition and image reconstruction using few frequency and spatial data observations. It was shown in [10] and in subsequent publications [10]–[12] that CS is a powerful tool in TWRI, provided that the scene is sparse or can be expressed in a sparse basis. However, both multipath ghosts and wall reverberations may cast a sparse scene as a populated scene, and at minimum will render the scene less sparse, degrading the performance of CS reconstruction. We propose various methods that directly incorporate multipath exploitation and wall-clutter mitigation into sparse signal reconstruction for stationary scenes. The goal is to suppress the multipath ghosts and at the same time increase the signal-to-clutter ratio (SCR). The wall effects are mitigated by mapping back multiple reflections within the wall and separating wall and target returns.

The proposed approach, in essence, deals with the issue of multipath and the application of CS. Multipath has been shown to affect radar imaging in urban scenarios [1], [13], [14]. Earlier work attempted to mitigate the adverse effects stemming from multipath propagation [1]. Subsequently, research has been conducted to utilize the additional information carried by the multipath returns. Kidera et al. [15] exploited the multipath returns to obtain information about shadowed parts of the target. Setlur et al. [5] considered multipath exploitation in TWRI, assuming prior knowledge of the interior and exterior wall layout. They developed a scheme taking advantage of the additional energy residing in the target ghosts. The authors form an image, calculate the locations of the ghosts for each target and map the ghosts back onto the corresponding target. In this way, the image becomes ghost-free with increased SCR. In contrast to this approach, in this paper, we calculate the propagation delays corresponding to different multipath returns for each assumed target position. Multipath returns associated with reflections from the same wall are grouped together and represented by one measurement matrix. This allows CS solutions to focus the returns on the true target positions without ghosting.

This same linear multipath formulation can be adopted for wall reverberations. CS solutions in this case would view the front wall reflections and wall reverberations as originally from the same pixels, but with different

delays. In so doing, wall reverberations will not affect the sparsity of the scene. Within the CS framework, wall mitigation techniques using full data volume were shown in [16], [17] to maintain their ability to attenuate front wall reverberations and contributions to radar returns when using reduced measurements. Other methods include projecting the measurements onto a space that does not contain the wall [18]. Unlike the above techniques, we introduce in this paper a novel idea for reconstructing both the target image and the wall. We show that the SCR can by increased by separating the two contributions, using models adapted to target and wall returns.

Compressive sensing (CS), on the other hand, has successfully been applied to TWRI, where the scene was described by a few point targets [10]. Subsequently, different aspects, e.g. the sparse representation of extended targets [12] or how to incorporate the wall returns [17], have been examined. Recently, multipath ghost suppression in SAR imagery has been studied in [19]. Tian et al. consider a far-field imaging scenario, where multipath results in a constant phase delay. They employ CS as an image post-processing step to separate the direct path targets from the multipath ghosts. We, however, consider multipath exploitation in near-field TWRI by formulating the image formation as a CS reconstruction problem.

Our main contribution is to develop a scheme joining multipath exploitation and compressive sensing. Relying on the established multipath signal model, we invert the model by means of sparse reconstruction. In this way, a simple and elegant formulation of the problem is provided and complex derivations for locating the ghosts, as in [5], are not needed. Moreover, we establish a novel scheme for mitigating the wall-clutter by a joint reconstruction of the wall an the target images. The effectiveness of our methods is shown using simulated and real data collected in a semi-controlled environment.

The remainder of the paper is organized as follows. In Sections II and III some basics for TWRI are reviewed and the multipath and wall propagation model is described. Subsequently, in Sections IV and V we present the CS reconstruction algorithms for multipath exploitation and wall-clutter mitigation. Results on simulated and measured data are discussed in Section VI. Finally, we will conclude the paper.

II. THROUGH-THE-WALL RADAR IMAGING FUNDAMENTALS

We focus on stepped-frequency ground radar operation and consider wideband delay and sum beamforming (DSBF) for through-the-wall image formation [1]. We note, however, that the CS multipath exploitation approach, proposed in this paper, is also applicable to both pulsed radar operation [11] and other imaging techniques in TWRI [8], [20], [21].

Assume that N wideband transceivers constitute a line array aperture, located parallel to the x-axis. The array is at a standoff distance from a homogeneous wall of thickness d. Let the stepped frequency signal consist of M frequencies, $\{f_m\}_{m=0}^{M-1}$, regularly spaced over the desired bandwidth $f_{M-1} - f_0$. Monostatic operation is assumed, i.e., when the mth transceiver is active, the reflections by the wall and any targets in the scene are measured only at the same transceiver location. The overall received signal, $y[m,n]$, corresponding to the mth frequency and the nth transceiver, can be expressed as the superposition of the target returns $y_t[m,n]$ and the wall response $y_w[m,n]$,

$$y[m,n] = y_t[m,n] + y_w[m,n]. \tag{1}$$

Suppose the region of interest or target space is divided into a regular grid with a finite number of grid points, with N_x and N_y, respectively, representing the points in crossrange and downrange. At the most, $N_x N_y$ point targets are assumed to reside on the spatial sampling grid. Let σ_p represent the complex reflectivity corresponding to the pth spatial grid point or the pth target, where $p = 0, 1, \ldots N_x N_y - 1$. Note that absence of a target at a particular grid point is simply represented by a zero value for the corresponding target reflectivity. Therefore, the target return $y_t[m, n]$ associated with transceiver n and frequency f_m can be expressed as,

$$y_t[m, n] = \sum_{p=0}^{N_x N_y - 1} \sigma_p \exp(-j2\pi f_m \tau_{pn}), \tag{2}$$

where τ_{pn} denotes the round-trip propagation delay between the p-th target and the n-th transceiver. The target reflectivities are assumed constant, independent of frequency and aspect angle. We assume knowledge or accurate estimation of the wall parameters, i.e., the thickness and the permittivity. Therefore, τ_{pn} can be calculated from geometric considerations, as will be explained in Section III. It is noted that inaccuracies in wall parameter estimates defocus the corresponding image and and cause the imaged targets to shift away from their true positions [22]. Several methods have been reported in the literature for accurate estimation of the relevant wall parameters [8], [23].

Due to the specular nature of the wall reflections, the nth transceiver will only receive reflections from the parts of the wall perpendicular to the incident wave [18]. Accordingly, the wall return $y_w[m, n]$ can be expressed as,

$$y_w[m, n] = \sigma_w \exp(-j2\pi f_m \tau_w), \tag{3}$$

where σ_w denotes the reflectivity of the wall observed by each antenna element and τ_w the two-way propagation delay from each antenna element to the front wall. As the monostatic array is parallel to the wall, the delay τ_w is independent of the variable n, as evident in the subscripts. In the case that the array axis bears a non-zero angle with the front wall, then the relative distance from each antenna to the wall can be equalized such that (3) is valid.

It is noted that the signal model does not account for wall reverberations and the target multipath returns. These will be incorporated in Section III.

A. Delay and Sum Beamforming

In order to generate an image of the scene of interest by using delay-and-sum beamforming, the MN measurements corresponding to M frequencies and N transceivers are processed as follows. The complex image value $I(x_p, y_p)$ at the pth grid point (x_p, y_p) is obtained by summing phase shifted copies of the MN signals [1], [24],

$$I(x_p, y_p) = \frac{1}{MN} \sum_{n=0}^{N-1} \sum_{m=0}^{M-1} y[m, n] \exp(j2\pi f_m \tau_{pn}), \tag{4}$$

where τ_{pn} is the focusing delay for the nth transceiver and the pth grid point. The set of delays $\tau_{p0}, \tau_{p1}, \ldots, \tau_{p(N-1)}$ align the radar returns received at the N antenna locations from the presumed target location (x_p, y_p). Note that delay-and-sum beamforming represented by (4) assumes a point target model for the scene and does not take into account the specular nature of the wall reflections.

III. MULTIPATH PROPAGATION MODEL

The through-the-wall propagation of electromagnetic waves from a transmitter to the target and back to a receiver is subject to distortions. In reaching the behind the wall target, the wave is refracted twice, once at the air-wall interface and then at the wall-air interface. The back scattered wave is again double refracted through the wall before reaching the receiver. We refer to this 'double-refracted on transmit and receive' return as the direct target return.

Multipath propagation corresponds to indirect paths, which involve reflections at one or more secondary reflectors, by which the signal may reach the target. Assuming diffuse target scattering, multipath returns can be broadly categorized as follows.

- *Interior Wall Multipath:* This involves indirect paths with reflection at one or more interior walls.
- *Floor/Ceiling Multipath:* These consist of returns involving secondary reflections from the floor and/or ceiling.
- *Wall Ringing Multipath:* This type involves signals that undergo multiple reflections within the front wall on transit to/from the target.
- *Target Interaction Multipath:* Multipath returns under this category include secondary paths that result from target-to-target interactions.

We only deal with interior wall and wall ringing multipath returns in this work. Floor/ceiling and target interaction multipath are not considered. The interior wall multipath returns can be further subdivided into the following classes:

- *First order multipath:* This involves a bistatic scattering scenario, where the signal propagation on transmit and receive takes place along different paths. This is the dominant case of multipath with one part of the round-trip path being the direct propagation to or from the target, and the other involving a secondary reflection at an interior wall.
- *Second order multipath:* This includes two cases. The first is a bistatic scattering scenario with one part of the round-trip path being the direct propagation to or from the target, and the other involving secondary reflections at two interior walls. The second is a monostatic scattering scenario wherein transmission and reception occurs along the same path, which involves a secondary reflection on an interior wall.
- *Higher-order multipath:* Higher-order interior wall multipath returns involving three or more secondary reflections during the round trip path are possible as well.

As the signal weakens at each secondary wall reflection, the second- and higher-order multipath returns can usually be neglected. Furthermore, for many presumed target locations, the corresponding propagation delay is high, and, most likely, would be equivalent to the direct-path delay of a target that lies outside the perimeter of the room being imaged. Thus, if necessary, this type of multipath, if exists, can be gated out.

In order to derive the multipath and wall refraction model, we assume perfect knowledge of the front wall, i.e. location, thickness, and permittivity, as well as the location of the interior walls. The derivation follows essentially from [1], [5].
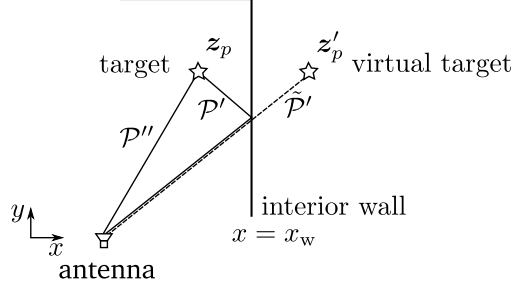
Fig. 1.   Multipath propagation via reflection at an internal wall.

A. Interior Wall Multipath

Consider the antenna-target geometry illustrated in Fig. 1, where the front wall has been ignored for simplicity. The pth target is located at $\boldsymbol{z}_p = [x_p, y_p]^T$, and the interior wall is parallel to the y-axis and located at $x = x_{\mathrm{w}}$. The multipath propagation consists of the forward propagation from the nth antenna to the target along the path $\mathcal{P}''$ and the return from the target via a reflection at the interior wall along the path $\mathcal{P}'$. Assuming the wall roughness to be much smaller than the wavelength, we can safely imply specular reflection. As a result, we observe from Fig. 1 that reflecting the return path about the interior wall yields an alternative antenna-target geometry. We obtain a virtual target located at $\boldsymbol{z}_p' = [2x_{\mathrm{w}} - x_p, y_p]^T$ and the delay associated with path $\mathcal{P}'$ is the same as that of the path $\tilde{\mathcal{P}}'$ from the virtual target to the antenna. This correspondence simplifies the calculation of the one-way propagation delay $\tau_{pn}^{(\mathcal{P}')}$ associated with path $\mathcal{P}'$. It is noted that this principle can be used for multipath via any interior wall.

From the position of the virtual target of an assumed target location, we can calculate the propagation delay along path $\mathcal{P}'$ as follows. Under the assumption of free space propagation, the delay can be simply calculated as the Euclidean distance from the virtual target to the receiver divided by the propagation speed of the wave. In the through-the-wall radar imaging scenario, however, the wave has to pass through the front wall on its way from the virtual target to the receiver. As the front wall parameters are assumed to be known, the delay can be readily calculated from geometric considerations using Snell's law [1].

B. Wall Ringing Multipath

When passing through the front wall, the wave is subject to reflections from the outer and inner surfaces of the wall. This causes multiple reflections within the wall, leading to what is referred to as wall ringing or reverberation [25]. Reverberation creates a set of propagation delays corresponding to the front wall, thereby causing the wall to appear in the image with associated replicas that are equally spaced in the downrange direction with exponentially decreasing amplitude. As part of the signal is transmitted beyond the wall at each inner-surface reflection, wall ringing has a similar effect on the target returns. That is, target copies that are equally spaced in the radial direction from the array are created in the image. We consider the wall ringing contribution on the target return in this section. The reverberation effects on the front wall return itself will be analyzed in Section V.
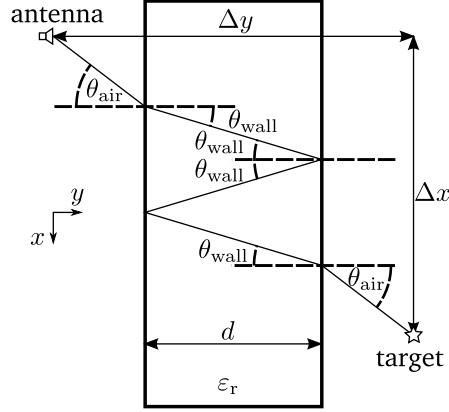
Fig. 2. Wall ringing propagation with $k = 1$ internal bounces.

The effect of wall ringing on the target image can be delineated through Fig. 2, which depicts the wall and the incident, reflected, and refracted waves. The distance between the target and the array element in crossrange direction, Δx, can be expressed as

$$\Delta x = (\Delta y - d) \tan \theta_{\text{air}} + d(1 + 2k) \tan \theta_{\text{wall}}, \tag{5}$$

where Δy is the distance between target and array element in downrange direction, and θ_{air} and θ_{wall} are the angles in the air and in the wall medium, respectively. The integer k denotes the number of internal reflections within the wall. The case $k = 0$ describes the direct path as derived in [1]. From Snell's law,

$$\frac{\sin \theta_{\text{air}}}{\sin \theta_{\text{wall}}} = \sqrt{\varepsilon_{\text{r}}}. \tag{6}$$

Equations (5) and (6) form a nonlinear system of equations that can be solved numerically for the unknown angles, e.g., using the Newton method. Having the solution for the incidence and refraction angles, we can express the one-way propagation delay associated with the wall ringing multipath as [25]

$$\tau(\Delta x, \Delta y, k) = \frac{(\Delta y - d)}{c \cos \theta_{\text{air}}} + \frac{\sqrt{\varepsilon_{\text{r}}} d(1 + 2k)}{c \cos \theta_{\text{wall}}}, \tag{7}$$

where c is the propagation speed in vacuum.

C. Received Signal Model

Having described the two principal multipath mechanisms in TWRI, namely the interior wall and wall ringing types of multipath, we are now in a position to develop a multipath model for the received signal. We assume that the front wall returns have been suppressed and the measured data contains only the target returns. The case with the wall returns present in the measurements will be handled in Section V.

Each path $\mathcal{P}$ from the transmitter to a target and back to receiver can be divided into two parts, $\mathcal{P}'$ and $\mathcal{P}''$, where $\mathcal{P}''$ denotes the partial path from the transmitter to the scattering target and $\mathcal{P}'$ is the return path back to the
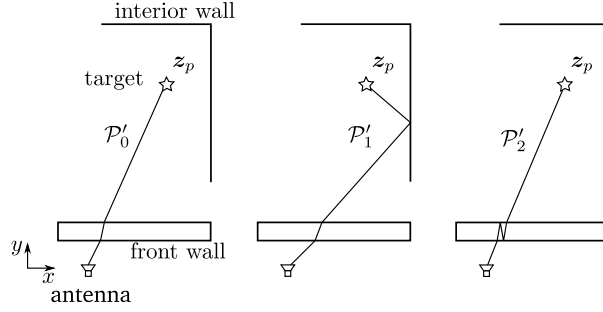
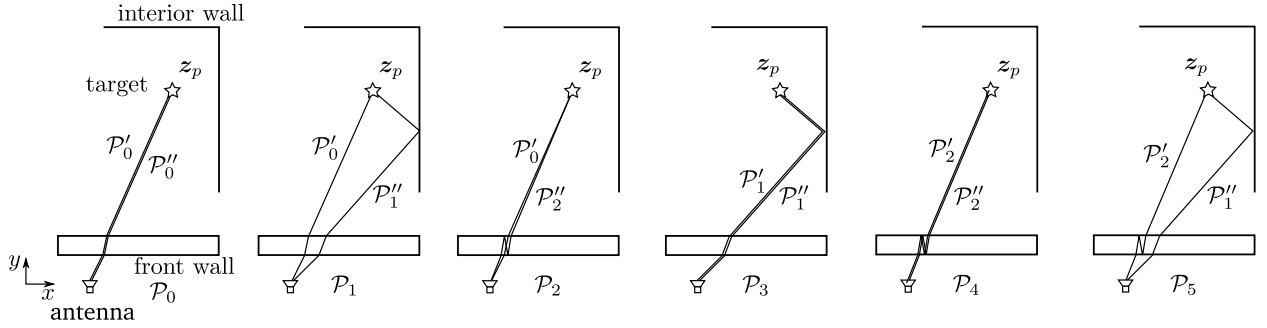Fig. 3. Example for three possible partial return paths.

Fig. 4. Unique round-trip paths between transceiver and target for the partial paths shown in Fig. 3

receiver. For each target-transceiver combination, there exist a number of partial paths due to the interior wall and wall ringing multipath phenomena. Let $\mathcal{P}'_{r_1}, r_1 = 0, \ldots, R_1 - 1$ and $\mathcal{P}''_{r_2}, r_2 = 0, \ldots, R_2 - 1$ denote the feasible partial paths. Any combination of $\mathcal{P}'$ and $\mathcal{P}''$ results in a round-trip path $\mathcal{P}_r, r = 0, \ldots, R - 1$. We can establish a function that maps the index r of the round-trip path to a pair of indices of the partial paths, $r \mapsto (r_1, r_2)$. Hence, we can determine the maximum number $R \leq R_1 R_2$ of possible paths for each target-transceiver pair. Note that, in practice, $R \ll R_1 R_2$, as some round-trip paths may be equal due to symmetry while some others could be strongly attenuated, and, thereby can be neglected. We follow the convention that $\mathcal{P}_0$ refers to the direct round-trip path. For illustration, consider Figure 3, which depicts three partial return paths, namely direct propagation, secondary reflection from a side wall, and path involving wall ringing. Note that the signal can also travel along the same paths on transmit. Considering these three partial paths for both transmission and reception leads to nine possible round-trip paths between the transceiver and the target. Since the order in which the signal propagates along two partial paths is not important, only six of the nine paths are unique and are shown in Figure 4. The last three paths in Figure 4 can be ignored because of higher attenuation.

The round-trip delay of the signal along path $\mathcal{P}_r$, consisting of the partial paths $\mathcal{P}'_{r_1}$ and $\mathcal{P}''_{r_2}$, can be calculated as

$$\tau_{pn}^{(\mathcal{P}_r)} = \tau_{pn}^{(\mathcal{P}'_{r_1})} + \tau_{pn}^{(\mathcal{P}''_{r_2})}. \tag{8}$$

Henceforth, for notational simplicity, we will denote the round-trip delay between the n-th array element and p-th target associated with path $\mathcal{P}_r$ as $\tau_{pn}^{(r)}$. It is noted that when a partial path corresponds to the wall ringing multipath, the corresponding delay will be given by (7). Likewise, we can calculate the complex amplitude $T_{pn}^{(\mathcal{P}_r)} \in \mathbb{C}$ associated with each possible round-trip path. The expressions for $T_{pn}^{(\mathcal{P}_r)}$ are derived in Appendix A and depend on the angles of incidence, the angles of refraction, and the dielectric properties of the front and interior walls.

In the following, we make two simplifications. First, provided that the incident, refraction, and reflection angles associated with a particular path do not significantly vary across the array, we can assume

$$T_{pn}^{(\mathcal{P}_r)} \approx T_p^{(\mathcal{P}_r)}, \quad n = 0, \ldots, N-1, \quad p = 0, \ldots, N_x N_y - 1. \tag{9}$$

In other words, complex amplitude factor for each path depends only on the assumed target location. The justification for this approximation is provided in Appendix B. Second, as the direct path is typically the strongest path under propagation through walls, we normalize all complex amplitudes to that of the direct path in order to avoid over-parameterization,

$$w_p^{(r)} = \frac{T_p^{(\mathcal{P}_r)}}{T_p^{(\mathcal{P}_0)}}, \quad r = 0, \ldots, R-1, \quad p = 0, \ldots, N_x N_y - 1 \tag{10}$$

Hence, from (8) and (9) we obtain a complex path weight $w_p^{(r)}$ for each possible path corresponding to the pth pixel, with the direct path having the weight $w_p^{(0)} = 1$.

Without loss of generality, we assume the same number of propagation paths for each pixel. The unavailability of a path for a particular pixel is reflected by a corresponding path weight of zero. The spatio-frequency received signal is a superposition of delayed and weighted versions, according to (8) and (10), of the transmitted signal corresponding to all possible propagation paths $r = 0, \ldots, R-1$, yielding

$$y[m,n] = y_{\mathrm{t}}[m,n] = \sum_{r=0}^{R-1} \sum_{p=0}^{N_x N_y - 1} w_p^{(r)} \sigma_p^{(r)} \exp(-j2\pi f_m \tau_{pn}^{(r)}). \tag{11}$$

As the bistatic radar cross section (RCS) of a target could be different from its monostatic RCS, the target reflectivity is considered to be dependent on the propagation path. For convenience, the path weight $w_p^{(r)}$ in (11) can be absorbed into the target reflectivity $\sigma_p^{(r)}$, leading to

$$y[m,n] = y_{\mathrm{t}}[m,n] = \sum_{r=0}^{R-1} \sum_{p=0}^{N_x N_y - 1} \sigma_p^{(r)} \exp(-j2\pi f_m \tau_{pn}^{(r)}). \tag{12}$$

Note that (12) is a generalization of the non-multipath propagation model (2). If the number of propagation paths is set to 1, then the two models are equivalent.

Using the delay and sum beamforming of (4), an image was generated from the described model and is shown in Fig. 5. The interior walls are superimposed on the image. The scene is chosen such that it mimics the available real data used later in Section VI. The target (circled) is located at (0.31, 3.6) m. We consider $R = 5$ round-trip propagation paths, where one partial path is always the direct path and the second partial path corresponds to: direct, back wall multipath, left side wall multipath, multipath w.r.t. the protruding right corner, and the wall
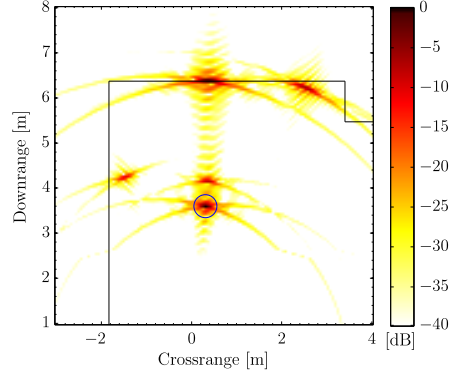
Fig. 5.   Beamformed image with ghost targets taking $R = 5$ propagation paths into account.

ringing multipath. The weightings of the paths are 1, 1, 0.3, 0.5 and 0.4, respectively, assuming that they vary only with the propagation path. The front wall lies at 2.4 m and has a thickness of 20 cm and a relative permittivity of 7.6. Observe that all false targets due to multipath, referred to as ghosts, lie within the room, thereby decreasing the sparsity of the scene.

D. Vectorized Measurements

The measurements in (12) can be vectorized for notational convenience. The measured data vector $\boldsymbol{y} \in \mathbb{C}^{MN \times 1}$ is obtained by stacking all MN measurements $y[m,n]$ in one column vector,

$$\boldsymbol{y} = [y[0,0], \ldots, y[M-1,0], \ldots, y[M-1, N-1]]^T. \tag{13}$$

The complex reflectivities $\sigma_p^{(r)}$ (merged with the path weights) corresponding to targets at positions $\boldsymbol{x}_p$ can be vectorized as,

$$\boldsymbol{s}^{(r)} = [\sigma_0^{(r)}, \sigma_1^{(r)}, \ldots, \sigma_{N_x N_y - 1}^{(r)}]^T. \tag{14}$$

Dictionary matrices $\boldsymbol{\Phi}^{(r)} \in \mathbb{C}^{MN \times N_x N_y}, r = 0, \ldots, R-1$, contain the phase terms and are defined by,

$$[\boldsymbol{\Phi}^{(r)}]_{ip} = \exp(-j2\pi f_m \tau_{pn}^{(r)}), \quad m = i \bmod M, n = \lfloor i/M \rfloor,$$
$$i = 0, 1, \ldots, MN - 1. \tag{15}$$

Now, using (13), (14), and (15), model (12) can be rewritten as

$$\boldsymbol{y} = \boldsymbol{y}_{\mathrm{t}} = \boldsymbol{\Phi}^{(0)} \boldsymbol{s}^{(0)} + \boldsymbol{\Phi}^{(1)} \boldsymbol{s}^{(1)} + \cdots + \boldsymbol{\Phi}^{(R-1)} \boldsymbol{s}^{(R-1)}. \tag{16}$$

The vectorized measurement model (16) will serve as the linear measurement equation for the CS reconstruction approach, described in the next section.

IV.   SPARSE SCENE RECONSTRUCTION WITH MULTIPATH EXPLOITATION

By employing compressive sensing, we, in essence, desire to achieve a good quality reconstruction of the sparse scene with efficient data acquisition, using only a subset of the full measurements. However, due to multipath

propagation, the imaged scene becomes populated by unwanted ghost targets which reduce the scene sparsity. Within the CS framework, we aim at undoing the ghosts, i.e., inverting the multipath measurement model and achieving a reconstruction, wherein only the true targets remain.

Various measurement schemes have been proposed in [10], [26]–[29] to reduce the volume of the acquired data. The common feature of all these schemes is that they can simply be expressed as a measurement or downsampling matrix $\boldsymbol{D} \in \mathbb{R}^{J \times MN}$ acting on the full set of measurements, where $J \ll MN$ is the number of reduced measurements. It is noted that in practical implementation of a CS radar, only a reduced number of measurements would be directly acquired, without the need for downsampling of the full set of measurements. For stepped-frequency operation, as considered in this work, a binary measurement matrix $\boldsymbol{D} \in \{0, 1\}^{J \times MN}$ is a reasonable choice [10], [26], [28]. In this case, one can think of $\boldsymbol{D}$ as an $MN \times MN$ identity matrix, where all but J rows have been deleted.

We obtain an undersampled measurement vector

$$\bar{\boldsymbol{y}} = \boldsymbol{D}\boldsymbol{y}. \tag{17}$$

Applying downsampling operation (17) to the model in (16) yields

$$\bar{\boldsymbol{y}} = \bar{\boldsymbol{y}}_{\mathrm{t}} = \boldsymbol{A}^{(0)}\boldsymbol{s}^{(0)} + \boldsymbol{A}^{(1)}\boldsymbol{s}^{(1)} + \cdots + \boldsymbol{A}^{(R-1)}\boldsymbol{s}^{(R-1)}, \tag{18}$$

where $\boldsymbol{A}^{(r)} = \boldsymbol{D}\boldsymbol{\Phi}^{(r)}, r = 0, 1, \ldots, R - 1$.

Having arrived at the reduced data model in (18), we now introduce different cases for casting the image formation process as a sparse reconstruction problem.

A. Group Sparse Reconstruction

In practice, any prior knowledge about the exact relationship between the various sub-images $\boldsymbol{s}^{(r)}$ of the sparse scene is either limited or nonexistent. However, we know with certainty that the sub-images $\boldsymbol{s}^{(0)}, \boldsymbol{s}^{(1)}, \ldots, \boldsymbol{s}^{(R-1)}$ describe the same underlying scene. That is, if a certain element in, e.g., $\boldsymbol{s}^{(0)}$ has a nonzero value, the corresponding elements in the other images should be also nonzero. In other words, the support of the R images is the same, or at least approximately the same. The common structure property of the sparse scene suggests the application of a group sparse or structured sparse reconstruction. We, therefore, propose a reconstruction approach based on group sparsity.

All unknown vectors in (18) can be stacked to from a tall vector $\tilde{\boldsymbol{s}} = \left[\left(\boldsymbol{s}^{(0)}\right)^T \ \left(\boldsymbol{s}^{(1)}\right)^T \ \cdots \ \left(\boldsymbol{s}^{(R-1)}\right)^T\right]^T \in \mathbb{C}^{N_x N_y R \times 1}$. The reduced measurement vector $\bar{\boldsymbol{y}}$ can then be expressed as

$$\bar{\boldsymbol{y}} = \tilde{\boldsymbol{A}}\tilde{\boldsymbol{s}}. \tag{19}$$

where the new measurement matrix has now the form $\tilde{\boldsymbol{A}} = [\boldsymbol{A}^{(0)} \ \boldsymbol{A}^{(1)} \ \cdots \ \boldsymbol{A}^{(R-1)}] \in \mathbb{C}^{J \times N_x N_y R}$.

We proceed to reconstruct the unknown reflectivity vectors or images $\tilde{\boldsymbol{s}}$ from the data record $\bar{\boldsymbol{y}}$ under measurement model (19). It has been shown that a group sparse reconstruction can be obtained by a mixed $\ell_1 - \ell_2$ norm

regularization [30]–[33]. Thus, we solve

$$\hat{\tilde{s}} = \arg\min_{\tilde{s}} \frac{1}{2} \|\bar{y} - \tilde{A}\tilde{s}\|_2^2 + \lambda\|\tilde{s}\|_{2,1}, \tag{20}$$

where

$$
\begin{aligned}
\|\tilde{s}\|_{2,1} :&= \sum_{p=0}^{N_x N_y - 1} \left\| \left[s_p^{(0)}, s_p^{(1)}, \ldots, s_p^{(R-1)} \right]^T \right\|_2 \\
&= \sum_{p=0}^{N_x N_y - 1} \sqrt{\sum_{r=0}^{R-1} s_p^{(r)} \left(s_p^{(r)} \right)^*}
\end{aligned}
\tag{21}
$$

and λ is the so-called regularization parameter. The convex optimization problem (20) can be solved using SparSA [30], YALL group [31], or other available schemes [33], [34]. SparSA uses a sequence of sub-problems that can be solved efficiently and converges to the overall optimum solution. YALL group is based on an alternating direction method (ADM), splitting the problem into two alternatingly solved subproblems. Both methods can be applied to large-scale problems, i.e., when matrix $\tilde{A}$ does not fit into memory. However, only Wright et al. give a proof of convergence for this type of problems [30].

The benefit of the group sparsity constraint or mixed norm regularization is the reduction of the degrees of freedom in the solution, and, as such, it enhances the recovery performance [31]. This remedies the R-fold increase in the number of unknowns due to the incorporation of multipath into the model formulation.

Once a solution $\hat{\tilde{s}}$ is obtained, the sub-images can be combined to form an overall image with improved signal-to-noise ratio (SNR). In the absence of any knowledge of the phase of the individual reflectivities $s_p^{(r)}$, a reasonable choice is a noncoherent combination. Hence, we obtain the final image by forming the Euclidean norm over each group. The elements of the composite image $\hat{s}_{\text{GS}}$ are defined by

$$[\hat{s}_{\text{GS}}]_p = \left\| \left[s_p^{(0)}, s_p^{(1)}, \ldots, s_p^{(R-1)} \right]^T \right\|_2, \quad p = 0, \ldots, N_x N_y - 1. \tag{22}$$

The noncoherent combination of the sub-images does not provide SNR gain, as the spatially white noise will also be accumulated. We are able, however, to enhance the signal-to-clutter ratio. By employing the aforementioned scheme (22), we ensure that the power scattered by the target, received via the direct path and multipath, is combined at the true location. Little or no power is added to the remaining ghosts or clutter, as they are not aligned across the sub-images. Hence, we expect a gain in the overall SCR as a result of noncoherent combination. It should be noted that the gain will be less if the path weights corresponding to the multipath returns are lower than 1. If the weight of a particular path is very low, it is more beneficial to disregard it in favor of SCR improvement and computational complexity.

B. Overlapping Group Sparse Reconstruction

The group sparse model described above can be generalized to overlapping group constraints. Instead of using non-overlapping groups of single pixels in each sub-image, the groups are extended to a neighborhood around each pixel. This is motivated by the observation that, in high-resolution images, targets are not perfect points but rather

Fig. 6.   Illustration of a first-order neighborhood grouping

occupy a number of adjacent pixels. The extend of the target in the image depends on its dimension and is also a function of the imaging system resolution in range and cross-range. This prior neighborhood information can be incorporated into the group sparse constraints. Additionally, we desire to include an intra-group weighting to allow application of a certain "tapering" to the groups. Towards this end, the mixed-norm term (21) can be replaced by the regularizer,

$$\rho(\tilde{s}) := \sum_{p=0}^{N_x N_y - 1} \sqrt{\sum_{r=0}^{R-1} \left\| \boldsymbol{W}^{(p)} s_{g_p}^{(r)} \right\|_2^2}, \tag{23}$$

where $g_p \subseteq \{0, 1, \ldots, N_x N_y - 1\}$ is an index set corresponding to the group of pixels forming a neighborhood around pixel p. The diagonal weighing matrix $\boldsymbol{W}^{(p)} \in \mathbb{R}^{|g_p| \times |g_p|}$ ensures that the weighting within a group is according to the desired pixel neighborhood relation. This yields the convex optimization problem

$$\hat{\tilde{s}} = \arg \min_{\tilde{s}} \frac{1}{2} \|\bar{\boldsymbol{y}} - \tilde{\boldsymbol{A}} \tilde{s}\|_2^2 + \lambda \rho(\tilde{s}). \tag{24}$$

Figure 6 illustrates how the grouping of the image pixels works. Assume we have an $N_x \times N_y = 10 \times 10$ pixel image and $R = 2$ possible propagation paths. The small number in the top left corner of each square indicates the pixel index, while the large number in the center represents the pixel weights of the depicted group. The index set for the group corresponding to the 12th pixel, as shown in the Figure, would be $g_{12} = \{2, 11, 12, 13, 22, 102, 111, 112, 113, 122\}$, where the second half of the set corresponds to indices in the multipath image ($r = 1$). The corresponding weighing matrix would be $\boldsymbol{W}^{(12)} = \frac{1}{2}\text{diag}\left(\frac{1}{8}, \frac{1}{8}, \frac{1}{2}, \frac{1}{8}, \frac{1}{8}, \frac{1}{8}, \frac{1}{8}, \frac{1}{2}, \frac{1}{8}, \frac{1}{8}\right)$. The index sets for all other groups are obtained similarly by shifting the cross-shaped mask to the appropriate pixel position. The weights should be chosen such that their sum is unity in order to avoid unintentional scaling of the reconstruction result.

The regularizer (23) in reconstruction problem (24) is not separable. That is, it cannot be expressed as a summation of functions of disjoint sets of its variables, and thus, cannot be solved by SparSA [30]. However, YALL group allows for overlapping groups and can be applied to the generalized group sparse reconstruction problem.

V. COMPRESSIVE SENSING RECONSTRUCTION INCLUDING THE WALL

In TWRI, the returns from the wall are very strong and can potentially mask the targets of interest. Within the CS framework, the wall poses an additional challenge. Being an extended target, the wall occupies many pixels in the image and, therefore, renders the scene less sparse. This will adversely affect the reconstruction performance when employing CS. Hence, different strategies for wall-removal or wall-clutter mitigation have been developed.

One approach is background subtraction [1], [35], where one assumes the availability of background data that can be coherently subtracted from the measurements of the populated scene. This method has been shown to work well in CS reconstruction [10], [12]. However, in real life scenarios, background measurements are typically not available and one has to resort to other means. A similar approach is change detection, where two consecutive or non-consecutive measurements of the same scene are coherently subtracted [11], [26], [36]. This scheme works well for revealing slowly moving targets; however, it fails for stationary scenes. For wall-clutter mitigation in stationary scenes, spatial filtering [6] and subspace projection [9] methods have been proposed, and have been successfully applied to CS reconstruction [17]. Another approach estimates the wall parameters from the first wave arrivals. The estimated parameters are used to model wall returns, which are subsequently subtracted from the total radar returns, rendering wall-free signals [8]. Although the effect of the use of a reduced number of frequency observations on the performance of the estimate, model, and subtract approach has not been investigated in the TWRI literature, a conceptually similar scheme under compressive measurements for the related problem of ground bounce removal in GPR was recently proposed in [37].

In this section, we follow a different approach wherein we reconstruct two images, one containing the targets and the other containing the wall. By using signal models adapted to diffuse targets and specular reflecting wall, we aim at separating the wall response from the target returns. We propose three different sparse reconstruction schemes that mitigate the wall response. The first scheme reconstructs the wall and the target scene separately. In the second scheme, we develop a joint reconstruction of the wall and the target scene using group sparse regularization. The third scheme generalizes the joint reconstruction by making use of additional prior knowledge through overlapping group sparse regularization.

A. Wall Reverberation Model

Foremost, a wall reverberation model is developed to make proper use of the structure of the wall return. The wall return including the ringing can be treated similar to the wall ringing target multipath. The major difference is that the wall reverberation does not involve any interaction with the targets in the scene of interest.

Each internal reflection within the wall can be considered as a wall return, similar to (3), from a different downrange. Hence, we establish a set of R_w possible paths and calculate the corresponding delays $\tau_\mathrm{w}^{(r)}$ according to (7) and path loss factors $a_r \in \mathbb{C}$ as explained in the Appendix A, where $r = 0, 1, \ldots, R_\mathrm{w} - 1$. The returns from all possible paths can be superimposed to form a wall reverberation measurement model, expressed as

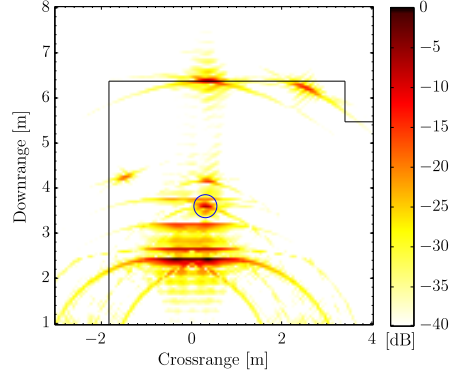$$y_\mathrm{w}[m, n] = \sum_{r=0}^{R_\mathrm{w}-1} a_r \sigma_\mathrm{w} \exp(-j2\pi f_m \tau_\mathrm{w}^{(r)}). \tag{25}$$

Fig. 7. Beamformed image with wall and ghost targets taking $R = 5$ and $R_\mathrm{w} = 4$ propagation paths into account.

Note that $\tau_\mathrm{w}^{(0)}$ describes the direct path and $\tau_\mathrm{w}^{(r)}$, $r > 0$, are the wall reverberation contributions. The decrease in amplitude for the higher order reverberation paths is accounted for in the loss factors $a_r \in \mathbb{C}$. Note that, in practice, due to the strong attenuation in wall materials, only two to three wall reverberation responses are typically observed [38].

A simulation of the beamformed image generated from the wall model (25) and the target model of Section III is shown in Fig. 7. The scene is the same as in the interior wall multipath example of Fig. 5. The first wall echo is assumed to be twice the amplitude of the target return and the wall reverberation damping factor is set to 0.4. For the wall model, $R_\mathrm{w} = 4$ propagation paths are considered. Observe that the first two returns lie at the inner and outer boundaries of the front wall; however, the higher order returns appear deeper inside the room.

For ease of notation and implementation, we use a modified wall model for the CS reconstruction. We equivalently assume the wall to be composed of small wall segments residing on the same grid as the targets. Despite modeling the wall as homogeneous, we allow for a different reflectivity for each wall pixel/segment. In this way, we obtain more flexibility in the image reconstruction, especially if perfect homogeneity of the wall is violated in the measurements. Then, we can express the vectorized wall reverberation model in a similar manner to (16) as

$$\boldsymbol{y}_\mathrm{w} = \boldsymbol{\Phi}_\mathrm{w}^{(0)} \boldsymbol{s}_\mathrm{w}^{(0)} + \boldsymbol{\Phi}_\mathrm{w}^{(1)} \boldsymbol{s}_\mathrm{w}^{(1)} + \cdots + \boldsymbol{\Phi}_\mathrm{w}^{(R_\mathrm{w}-1)} \boldsymbol{s}_\mathrm{w}^{(R_\mathrm{w}-1)}, \qquad (26)$$

where $\boldsymbol{s}_\mathrm{w}^{(r)}$ are the vectorized reflectivities of the wall segments incorporating the loss factors a_r and $\boldsymbol{\Phi}_\mathrm{w}^{(r)}$ contains the phase information for path r. The matrices $\boldsymbol{\Phi}_\mathrm{w}^{(r)}$ are essentially the same as $\boldsymbol{\Phi}^{(r)}$, except that the unwanted contributions violating the specular reflection assumption are masked out. That is,

$$\boldsymbol{\Phi}_\mathrm{w}^{(r)} = \boldsymbol{M} \circ \boldsymbol{\Phi}^{(r)}, \qquad (27)$$

where '$\circ$' denotes the element wise or Schur product and $\boldsymbol{M} \in \{0, 1\}^{MN \times N_x N_y}$ is a binary matrix. An element $[\boldsymbol{M}]_{pn}$ assumes a unit value if the p-th wall segment is visible to the n-th array element and zero otherwise. In other words, the contribution from all specular targets that are not directly in front of the antenna are masked out by $\boldsymbol{M}$. Definition (27) typically results in a wall dictionary matrix $\boldsymbol{\Phi}_\mathrm{w}^{(r)}$ that contains many zeros [18].

For the CS reconstruction, analogous to (1), we consider the downsampled superposition of the target and wall contributions to the measured signal,

$$\bar{y} = \bar{y}_\text{t} + \bar{y}_\text{w} = D y_\text{t} + D y_\text{w}. \tag{28}$$

where the target contribution $\bar{y}_\text{t}$ is defined in (18). For the wall response, we obtain from (26)

$$\bar{y}_\text{w} = A_\text{w}^{(0)} s_\text{w}^{(0)} + A_\text{w}^{(1)} s_\text{w}^{(1)} + \cdots + A_\text{w}^{(R_\text{w}-1)} s_\text{w}^{(R_\text{w}-1)}, \tag{29}$$

where $A_\text{w}^{(r)} = D \Phi_\text{w}^{(r)}, r = 0, 1, \ldots, R_\text{w} - 1$.

B. Separate Reconstruction

The first and somewhat simplistic approach is to reconstruct the wall and target images separately. This is mainly done for comparison so as to demonstrate that more sophisticated reconstruction approaches would provide higher benefits.

For the reconstruction, we can choose one of the methods described in Section IV. We apply the chosen method to the measurements $\bar{y}$ twice, once using the target model in (18) and once using the wall model in (29). Hence, we obtain two images, $\hat{s}$ and $\hat{s}_\text{w}$, describing the targets and the wall, respectively. Note that the two reconstructions are independent in the sense that no information from the wall image is used to form the target image and vice versa.

C. Joint Group Sparse Reconstruction

As a second approach, we reconstruct the wall and target images by using the group sparse approach as described in Section IV-A. We join the two models (18) and (29) resulting in

$$\bar{y} = \tilde{A}_\text{j} \tilde{s}_\text{j}, \tag{30}$$

where the vector $\tilde{s}_\text{j} \in \mathbb{C}^{N_x N_y (R+R_\text{w}) \times 1}$ is obtained by stacking the various vectors of the scene of interest as

$$\tilde{s}_\text{j} = \left[\left(s^{(0)} \right)^T \cdots \left(s^{(R-1)} \right)^T \left(s_\text{w}^{(0)} \right)^T \cdots \left(s_\text{w}^{(R_\text{w}-1)} \right)^T \right]^T, \tag{31}$$

and the new measurement matrix $\tilde{A}_\text{j} \in \mathbb{C}^{J \times N_x N_y (R+R_\text{w})}$ has the form

$$\tilde{A}_\text{j} = [A^{(0)} \ A^{(1)} \ \cdots \ A^{(R-1)} \ A_\text{w}^{(0)} \ A_\text{w}^{(1)} \ \cdots \ A_\text{w}^{(R_\text{w}-1)}]. \tag{32}$$

From the above high-dimensional joint model of Eqns. (30) to (32), we can pose the reconstruction problem using a group sparse regularization term. The convex optimization problem is essentially the same as in (20)

$$\hat{\tilde{s}}_\text{j} = \arg \min_{\tilde{s}_\text{j}} \frac{1}{2} \| \bar{y} - \tilde{A}_\text{j} \tilde{s}_\text{j} \|_2^2 + \lambda \rho_\text{j}(\tilde{s}_\text{j}), \tag{33}$$

where

$$\rho_\text{j}(\tilde{s}_\text{j}) := \sum_{p=0}^{N_x N_y - 1} \left\| \left[s_p^{(0)}, s_p^{(1)}, \ldots, s_p^{(R-1)} \right]^T \right\|_2$$
$$+ \sum_{p=0}^{N_x N_y - 1} \left\| \left[s_{\text{w},p}^{(0)}, s_{\text{w},p}^{(1)}, \ldots, s_{\text{w},p}^{(R_\text{w}-1)} \right]^T \right\|_2. \tag{34}$$

TABLE I

MUTUAL COHERENCE FOR IMAGE RESOLUTION 64×64

Meas.	$\bar{A}$	$\bar{A}_{\mathrm{w}}$	$\bar{A}_{\mathrm{wr}}$	$\bar{A},\bar{A}_{\mathrm{w}}$	$\bar{A},\bar{A}_{\mathrm{wr}}$
12%	0.883	0.977	0.903	0.750	0.575
6%	0.883	0.996	0.981	0.777	0.619
3%	0.889	0.996	0.977	0.779	0.622

TABLE II

MUTUAL COHERENCE FOR IMAGE RESOLUTION 32×32

Meas.	$\bar{A}$	$\bar{A}_{\mathrm{w}}$	$\bar{A}_{\mathrm{wr}}$	$\bar{A},\bar{A}_{\mathrm{w}}$	$\bar{A},\bar{A}_{\mathrm{wr}}$
12%	0.593	0.823	0.597	0.742	0.562
6%	0.605	0.908	0.697	0.768	0.604
3%	0.615	0.900	0.686	0.769	0.609

The difference lies in the choice of the regularizer (34). Our choice stems from the fact that the wall sub-images should all share the same support and all target sub-images should have a common support, different from that of the wall sub-images. The difference in supports of the wall and target images is due to the fact that the two capture different characteristics of the scene. This is achieved by grouping the pixels of the target and wall sub-images separately.

Note that in (30), we essentially extend the measurement or dictionary matrix to contain both the target and wall atoms for all possible paths in its columns. In doing so, we can express sparsely the wall and target contributions in $\bar{y}$. However, as the wall and target measurement matrices are very similar, we expect considerable mutual coherence between their columns. This will likely impair the reconstruction in (33) and the target and wall images may not be fully separated.

The mutual coherence of the measurement matrix is a measure of the correlation between its columns. A matrix with low mutual coherence is well suited to obtain a unique reconstruction from a few measurements [39]. We examined the mutual coherence of the target matrix $\bar{A}$ and wall matrix $\bar{A}_{\mathrm{w}}$ as well as the mutual coherence between the two matrices.. Only the case of non-multipath propagation was investigated, i.e. $\bar{A} = A^{(0)}$ and $\bar{A}_{\mathrm{w}} = A_{\mathrm{w}}^{(0)}$, however, we expect similar results for the multipath case. Additionally, we examined the mutual coherence when we restricted the wall model to a small downrange region around the known position of the front wall, resulting in matrix $\bar{A}_{\mathrm{wr}}$. The results, averaged over 100 Monte Carlo runs, are listed for various undersampling ratios and two different image resolutions in Tables I and II. It is clear, that $\bar{A}$ and $\bar{A}_{\mathrm{w}}$ have a very high mutual coherence, which stems from oversampling in the image domain. Observe that the mutual coherence decreases when using a lower image resolution. The mutual coherence between the target and wall matrices is lower than that of the self-coherence values, yet still rather high. Hence, we expect that we can separate wall and targets to a certain extent, however, not perfectly.

Having obtained a solution $\hat{\bar{s}}_{\mathrm{j}}$ from (33), we need to combine the target sub-images to form a single composite

Fig. 8.   Illustration of a neighborhood grouping matched to walls

target image and likewise for the wall sub-images. As explained in Section IV, a natural choice is to combine the sub-images using the Euclidean norm over the corresponding pixels. This is done separately for the target image $\hat{\tilde{s}}_{\mathrm{GS}}$ and the wall image $\hat{\tilde{s}}_{\mathrm{GS,w}}$ in the same fashion as (22).

D. Joint Overlapping Group Sparse Reconstruction

Finally, we reconstruct the wall and target images by using the overlapping group sparse approach as described in Section IV-B. This is a generalization of the non-overlapping groups in the previous subsection and allows more flexibility. Hence, we can include appropriate prior knowledge, i.e. neighborhood information, about the target and wall images separately. For the target sub-images, a first-order neighborhood might be a good choice, as explained in Section IV-B. However, we know that, for the wall sub-images, the wall pixels form lines along the crossrange direction. Hence, a group structure that promotes pixel groups elongated in crossrange direction and short in downrange direction should be chosen.

Bearing in mind the above considerations, we can solve (33) by replacing the regularizer with

$$
\begin{aligned}
\rho_{\mathrm{j}}(\tilde{s}_{\mathrm{j}}) := & \sum_{p=0}^{N_x N_y - 1} \sqrt{\sum_{r=0}^{R-1} \left\| \boldsymbol{W}_{\mathrm{t}}^{(p)} s_{g_p}^{(r)} \right\|_2^2} \\
& + \sum_{p=0}^{N_x N_y - 1} \sqrt{\sum_{r=0}^{R_{\mathrm{w}}-1} \left\| \boldsymbol{W}_{\mathrm{w}}^{(p)} s_{\mathrm{w},h_p}^{(r)} \right\|_2^2},
\end{aligned}
\tag{35}
$$

where the first term in (35) ensures the proper regularization for the target images and the second term for the wall images. Analogous to the target only case, $g_p, h_p \subseteq \{0, 1, \ldots, N_x N_y - 1\}$ are index sets corresponding to the group of pixels forming a neighborhood around pixel p. The diagonal weighting matrices $\boldsymbol{W}_{\mathrm{t}}^{(p)} \in \mathbb{R}^{|g_p| \times |g_p|}, \boldsymbol{W}_{\mathrm{w}}^{(p)} \in \mathbb{R}^{|h_p| \times |h_p|}$ ensure the weighting within a group according to the desired pixel neighborhood relation.

Figure 8 illustrates an example of the pixel grouping for walls. Again, the small number in the top left corner of each square indicates the pixel index and the large number in the center is the pixel weight of the depicted group. Assume we have an $N_x \times N_y = 10 \times 10$ pixel image and $R_{\mathrm{w}} = 2$ possible propagation paths. The index set for the 12th group, as shown in the Figure, would be $h_{12} = \{2, 12, 22, 102, 112, 122\}$, where the second part of
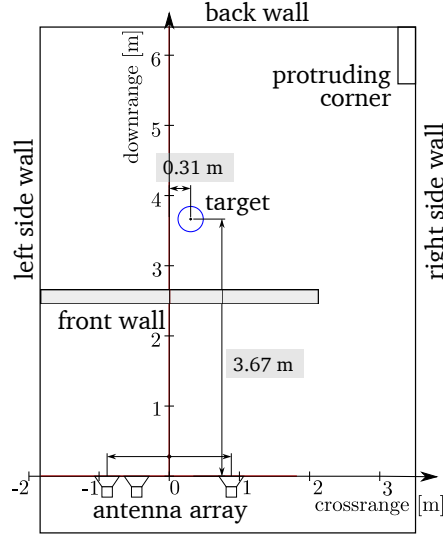
Fig. 9.   Measurement setup and room layout

the set corresponds to indices in the wall reverberation image ($r = 1$). The corresponding weighing matrix would be $\boldsymbol{W}_{\text{w}}^{(12)} = \frac{1}{2}\text{diag}\left(\frac{1}{8}, \frac{3}{4}, \frac{1}{8}, \frac{1}{8}, \frac{3}{4}, \frac{1}{8}\right)$. The index sets for all other groups are obtained similarly by shifting the rectangular mask to the appropriate pixel position.

VI. Results

For both simulation and experiments, we assume the same measurement setup and room layout, which is depicted in Fig. 9. A 77-element uniform linear monostatic array with an inter-element spacing of 1.9 cm is used for imaging. The origin of the coordinate system is chosen to be at the center of the array. The concrete front wall is located parallel to the array at 2.44 m downrange and has a thickness $d = 20$ cm and relative permittivity $\epsilon = 7.6632$. The left sidewall is at a crossrange of -1.83 m, whereas the back wall resides at 6.37 m downrange. Also, there is a protruding corner on the right at 3.4 m crossrange and 4.57 m downrange. A stepped-frequency signal, consisting of 801 equally spaced frequency steps covering the 1 to 3 GHz band is employed for scene interrogation.

A. Simulation Results

First, we simulate two point targets, located at (0.31, 3.6) m and (-0.62, 5.2) m, without considering the returns from the front wall. We consider the same propagation paths as in the example in Section III (Fig. 5). White noise with 0 dB SNR is added to the simulated measurements, i.e. $\bar{\boldsymbol{y}}_{\text{noisy}} = \bar{\boldsymbol{y}} + \boldsymbol{n}$ with the SNR defined as SNR $= 20\log_{10}(\|\bar{\boldsymbol{y}}\|_2/\|\boldsymbol{n}\|_2)$. For comparison, the beamformed image using the full data record is depicted in Fig. 10a. For all other parts of Fig. 10 corresponding to CS, we use only one-fourth of the array elements and one-eighth of the frequencies for scene reconstruction, both sets are chosen at random. The CS results, shown in Fig. 10, are averaged over 100 Monte Carlo runs.

(a) Conventional DSBF
(b) Conventional CS
(c) Non-overlapping GSCS

(d) Overlapping GSCS
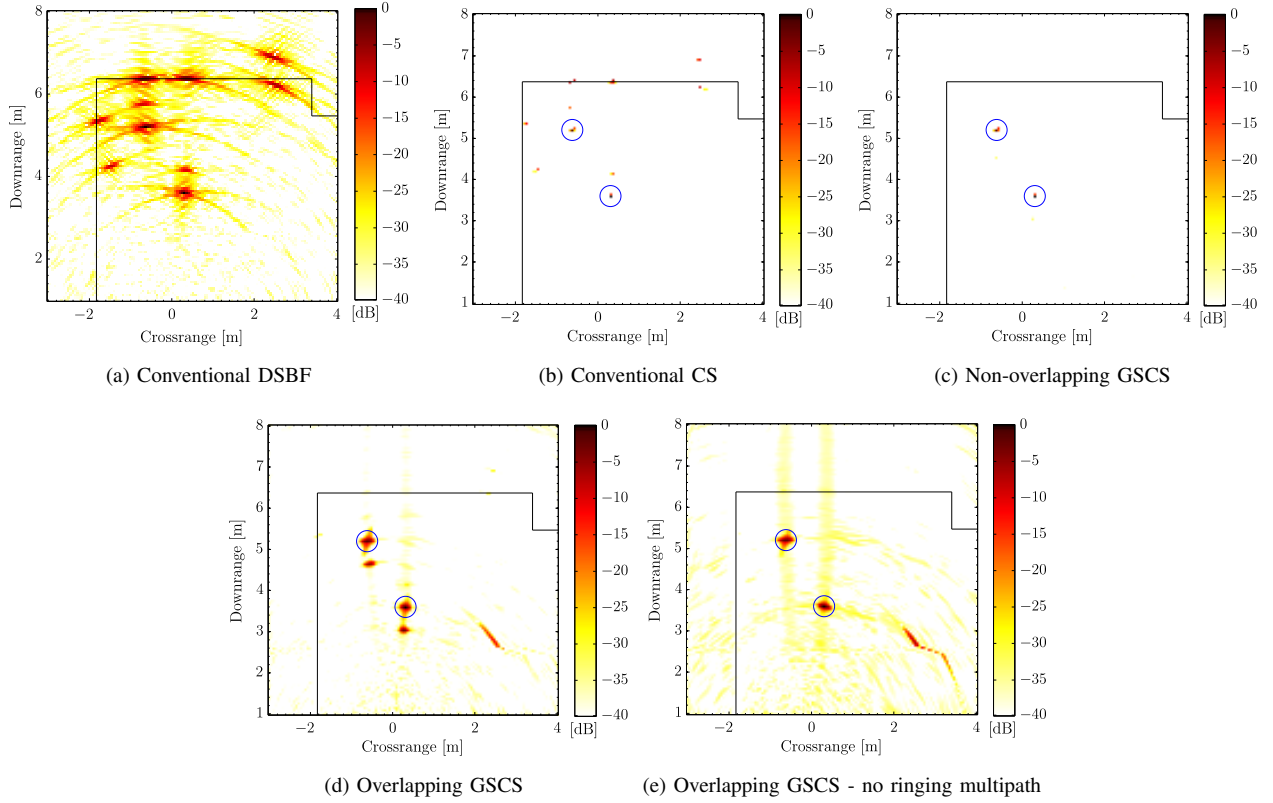(e) Overlapping GSCS - no ringing multipath

Fig. 10. Reconstruction results using different algorithms for the simulated scene with two point targets. One fourth of the array elements and one eighths of the frequency bins were used for the formation of (b) - (e). Image (a) was created using the full set of measurements.

Fig. 10b shows the reconstruction result using conventional CS approach which does not exploit multipath [10]. It is observed that all ghost targets are reconstructed, which make the scene highly cluttered. The group sparse reconstruction approach, shown in Fig. 10c, provides a superior performance by suppressing all the ghosts. In Fig. 10d, we display the result of the overlapping group sparse reconstruction. Evidently, there are some reconstruction artifacts that appear at downranges slightly closer to the array than the targets. This is due to the ambiguities resulting from the wall ringing multipath, which, in effect, causes the algorithm to consider the true targets as multipath ghosts leading to inferior performance as compared to the non-overlapping approach. This effect is demonstrated in Fig. 10e, which corresponds to the case where the wall ringing multipath was omitted from the simulation model, and the artifacts are considerably reduced.

Next, the quantitative performance of the proposed reconstruction algorithms is investigated. To this end, we use two different metrics, namely, the SCR and the relative clutter peak (RCP). The SCR is defined as the ratio between the maximum target amplitude and the average amplitude in the clutter region [6]. We define the clutter region as the area within the room, excluding circular regions of radii 20 cm at the known target positions. On the other hand, the RCP equals the maximum target amplitude divided by the maximum clutter amplitude. Both quality metrics favor clean images with low noise and clutter power and high target amplitudes. The RCP metric especially
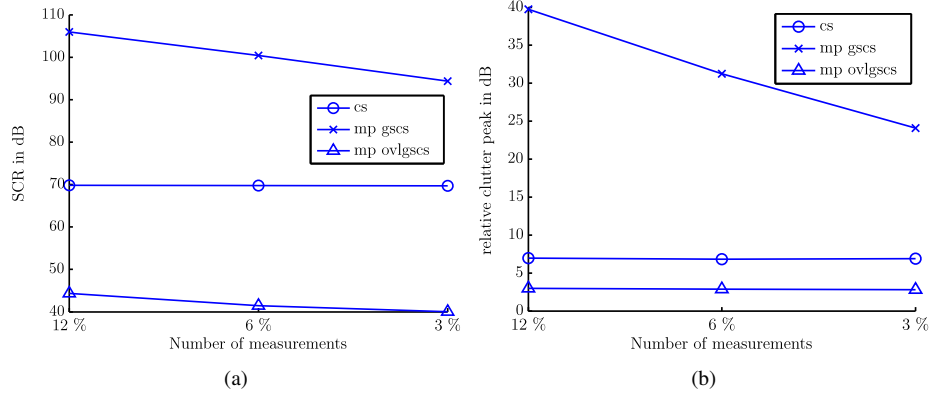
Fig. 11. Reconstruction performance vs. number of measurements for various algorithms.

penalizes strong clutter or ghost targets, which, in turn, can lead to false alarms in a subsequent detection step.

Figure 11 depicts the two metrics vs. undersampling ratio for various proposed algorithms. The conventional CS reconstruction without multipath exploitation ("cs") serves as a benchmark for these performance evaluations. The best performance is achieved by the non-overlapping group sparse approach ("mp gscs") w.r.t. both metrics. On the other hand, the overlapping group sparse approach ("mp ovlgscs") performs worse than the conventional CS reconstruction w.r.t. the considered metrics. For the SCR, the performance degradation of the overlapping group sparse approach is attributed to the residual clutter and noise visible in Fig. 10d, whereas the RCP is reduced due to the artifacts (false targets) in the reconstructed image. In summary, the proposed non-overlapping group sparse approach significantly outperforms the conventional CS reconstruction, whereas the overlapping variant is lacking in performance due to pronounced residuals in the formed image.

Subsequently, a simulation is carried out using the same scene, but with the front wall returns retained in the measurements. Reflections from the front face of the wall as well as three wall reverberations are considered, resulting in a total of four propagation paths for the wall model. The target model is kept unaltered. Again, white noise with 0 dB SNR is added to the simulated measurements. For comparison, the beamformed image using the full data record is depicted in Figure 12. For the proposed CS reconstructions, we use one-fourth of the array elements and one-fourth of the frequencies. The corresponding results, averaged over 100 Monte Carlo runs, are provided in Fig. 13.

Separate reconstruction of the wall and target images with multipath exploitation is carried out using the group sparse reconstruction approach. Note that for the wall image, both in separate and subsequent joint reconstructions, the first reverberation corresponding to the return from the back face of the wall is treated as a valid target and not as a multipath return and as such it becomes visible in the reconstructed wall images. The targets get reconstructed along with the wall, as seen in Fig. 13a. The ghost targets are suppressed, however, some clutter pixels remain in the reconstructed image. Hence, the relative clutter peak remains at a value of 5.8 dB.

Next, we employ joint group sparse CS reconstruction with non-overlapping groups as described in Section V-C. As shown in Fig. 13c, we achieve a very clean reconstruction of the two targets, leading to an RCP of 17.2 dB.
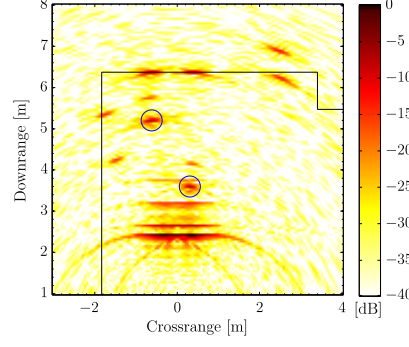
Fig. 12.   Conventional DSBF reconstruction of the simulated scene including the wall response.

(a) Separate Rec., Target

(c) Joint Non-overlapping GS Rec., Target

(e) Joint Overlapping GS Rec., Target

(b) Separate Rec., Wall

(d) Joint Non-overlapping GS Rec., Wall
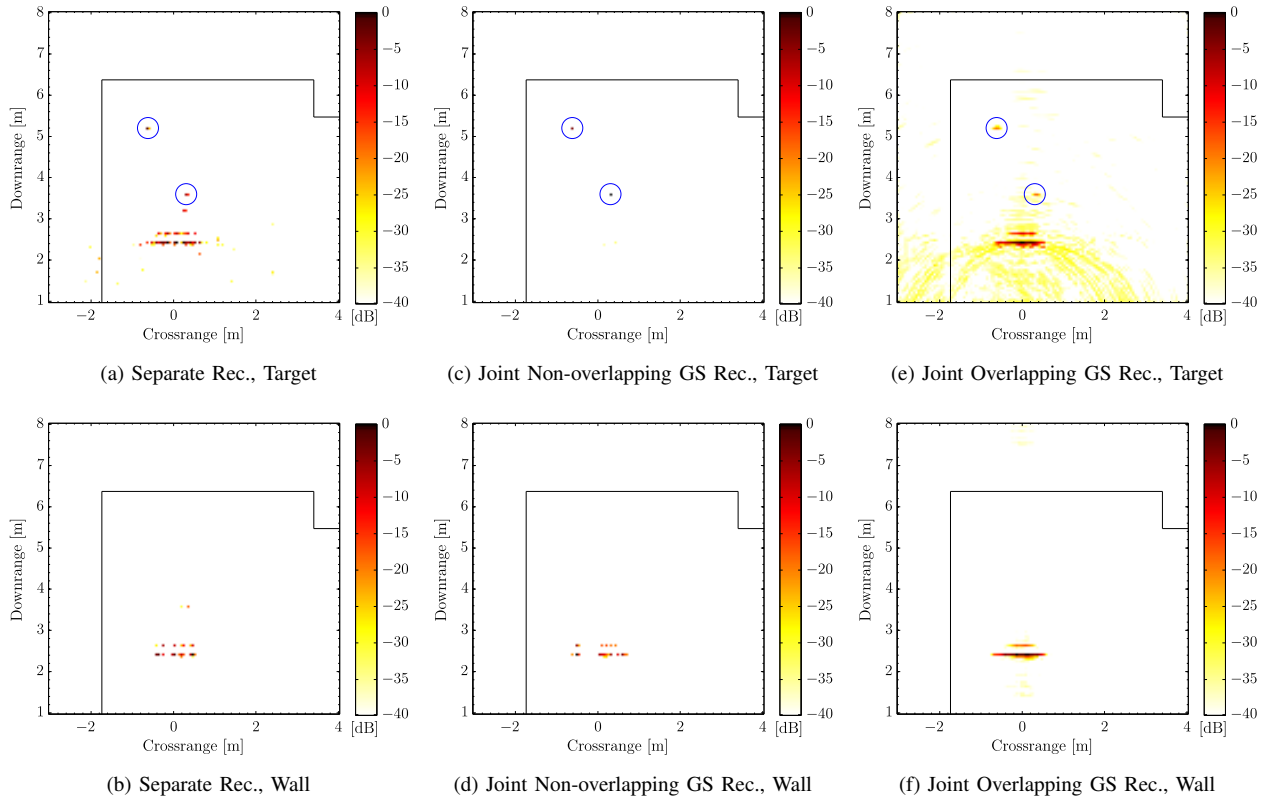
(f) Joint Overlapping GS Rec., Wall

Fig. 13.   Reconstruction results using different algorithms for the simulated scene including the wall response. One fourth of both the array elements and frequency bins were used for the image formation.

The ghost targets and the wall returns are well suppressed. In Fig. 13e the reconstruction using the overlapping group sparse approach is depicted, where RCP is 15 dB. Observe that the ghost targets get suppressed, however, the wall and some noise, mainly before the wall, remain. The reconstruction of the wall image is very similar for separate and joint group sparse CS reconstruction, refer to Figs. 13b,d. In both results, the wall appears as isolated pixels, roughly aligned in two lines. By using the overlapping group sparse method, the depiction of the wall in Fig. 13f is much smoother and appears as a single contiguous area. This improvement is due to the group sparse
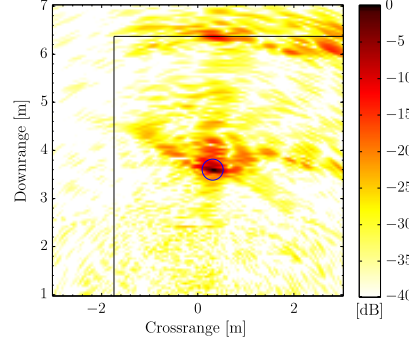
Fig. 14. Conventional DSBF reconstruction of the Al pipe scene.

(a) Simple CS rec.　　　　　(b) Non-overlapping GSCS　　　　　(c) Overlapping GSCS
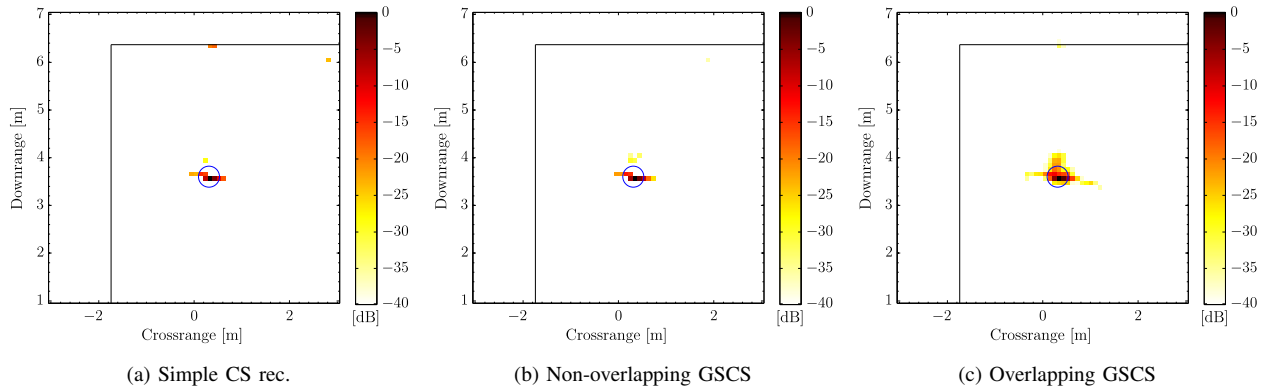
Fig. 15. Reconstruction results using different algorithms for the Al pipe scene. One fourth of the array elements and half of the frequency bins were used for the image formation.

regularization in the wall model, promoting smooth and elongated structures.

It can be concluded from the aforementioned simulation results that the sophisticated joint reconstruction has a significant advantage over separate reconstruction. Indeed, using the joint non-overlapping group sparse approach, we achieve almost perfect separation and reconstruction of the target and wall scenes. In the case of the joint overlapping group sparse approach, multipath ghosts are suppressed, however, some energy from the wall image leaks into the target scene.

B. Experimental Results

To complement and verify the simulation results, an experiment was conducted in a semi-controlled environment at the Radar Imaging Lab, Villanova University. A single aluminum pipe (61 cm long, 7.6 cm diameter) was placed upright on a 1.2 m high foam pedestal at 3.67 m downrange and 0.31 m crossrange. The left and right side walls were covered with RF absorbing material, but the protruding right corner and the back wall were left uncovered. For now, we consider background subtracted data to focus only on target multipath.

Figure 14 depicts the beamformed image using all available data. Apparently, only the multipath ghosts due to
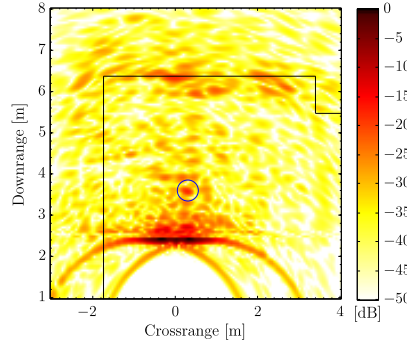
Fig. 16. Conventional DSBF reconstruction of the Al pipe scene without using background subtraction.

the back wall, and the protruding corner in the back right are visible. Hence, we only consider these two multipath propagation cases for our proposed schemes. In order to achieve efficient data collection, in the following, one-fourth of the array elements and one-half of the frequencies are used. The conventional CS reconstruction is shown in Fig. 15a, where the wall multipath ghost is still visible. The group sparse reconstructions with multipath exploitation are capable of suppressing this ghost, see Figs. 15b,c. Observe the smoother depiction of the target when using overlapping groups. The conclusions obtained by eye inspection are also backed by the corresponding RCP values. For conventional CS, the RCP is 46.5 dB, whereas the quality metric improves to 66.5 dB and 64 dB, for non-overlapping and overlapping group sparse reconstructions, respectively. Note that the target mask was increased to 50 cm radius, so that no part of the target response is treated as clutter.

Next, the wall and target separation performance of the proposed algorithms is investigated. We consider the same scene with a single aluminum pipe as described above, however, we do not use background subtraction. In order to suppress the antenna mismatch response, a hamming window over the frequencies is used and data samples corresponding to low (up to the front wall) and high delays (well behind the back wall), which contain no target information, are gated out.

Figure 16 depicts the beamformed image using all available data. Observe that the wall response is about 15 dB stronger than the target. The response from the front side and the back side of the wall along with multipath propagation via the back wall are clearly visible. Hence, we use the proposed algorithms considering the direct path and one multipath via the back wall. The undersampling ratio is kept at the same level as for the previous experiment. In Figure 17a,b, the separate CS reconstruction of the target and wall scene is shown, where the RCP is 12.5 dB. The relative clutter peak for the joint reconstruction with non-overlapping group sparse regularization is 10.9 dB, see Fig. 17c. Additionally, the image appears cleaner as clutter and the wall response are suppressed more effectively, leading to an SCR improvement of about 7 dB. When using the joint reconstruction with overlapping group sparse regularization, refer to Fig. 17e, the target becomes more visible as it covers more pixels and the RCP improves to 14.3 dB. However, at the same time, the clutter in the room becomes more pronounced and the wall is strongly leaking into the target image. Therefore, both separate and joint reconstruction algorithms are unable
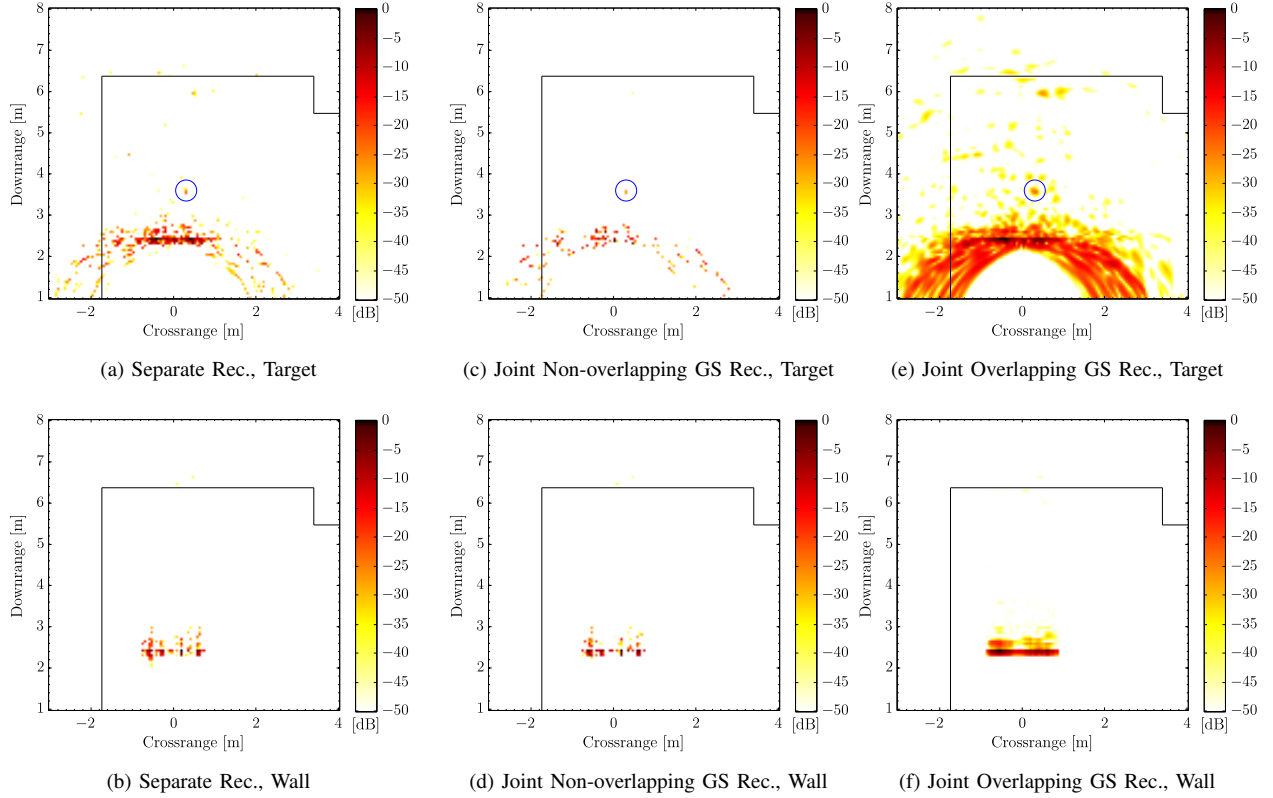
(a) Separate Rec., Target

(c) Joint Non-overlapping GS Rec., Target

(e) Joint Overlapping GS Rec., Target

(b) Separate Rec., Wall

(d) Joint Non-overlapping GS Rec., Wall

(f) Joint Overlapping GS Rec., Wall

Fig. 17. Reconstruction results using different algorithms for the Al pipe scene without background subtraction. One fourth of the array elements and half of the frequency bins were used for the image formation.

to separate the wall and the target responses in a satisfactory manner. The best performance is achieved by joint non-overlapping group sparse regularization, where the wall response is significantly stronger in the wall scene, Fig. 17d, as compared to the target scene, Fig. 17c.

The limited capability to separate the wall and the target responses can be attributed to i) residual sidelobe leakage of the very strong antenna mismatch response, and ii) the construction of the front wall. The wall is constructed by stacking solid concrete blocks without any mortar and there is no plaster, resulting in a wall that does not have a smooth surface and has air gaps. Therefore, the assumptions of homogeneity and specular reflection for the front wall are violated. This, in turn, impairs the ability of separating the wall and target responses using the proposed CS algorithms. Hence, we observe significant "cross-talk" between the wall and target images.

VII. CONCLUSION

In this paper, we presented a combined multipath and wall reverberation model for TWRI applications. Based on the proposed model, group sparse reconstruction methods under efficient data collection were proposed towards the objective of reconstructing the ground truth of the image without multipath ghosts and wall reverberations. Both overlapping and non-overlapping groups were considered. For the overlapping groups, a regularization adapted to prior knowledge of the neighborhood relation in the image was discussed, and shown to be beneficial for wall

reconstruction. Scene reconstruction under 'multipath only' and 'multipath plus reflections and reverberations from wall' cases were separately analyzed. For the latter case, the incorporation of the wall reverberations and direct returns into the CS formulation removed any need for further wall mitigation. By using two measurement models, one adapted to the target and one to the wall signal, we were able to reconstruct two images, separating, at least to a certain extent, the wall and the target information. Using numerical simulation and experimental data, the proposed techniques were shown to suppress ghosts, thereby increasing the signal-to-clutter ratio or relative peak clutter at the true target locations.

APPENDIX A

COMPLEX AMPLITUDE DERIVATION

For each path, the complex amplitude $T_{pn}^{(\mathcal{P}_r)}$ can be derived from the dielectric properties of the front and interior walls and the corresponding angles of incidence and refraction. A path $\mathcal{P}_r$ consists of two partial paths, $\mathcal{P}'_{r_1}$ and $\mathcal{P}''_{r_2}$, describing the propagation from the transceiver to the target and from the target back to the transceiver, respectively. Therefore, the complex amplitude associated with the total path equals the product of the complex amplitudes of the two partial paths, each consisting of one transmission coefficient associated with the front wall and one reflection coefficient, resulting in [40]

$$T_{pn}^{(\mathcal{P}_r)} = T_{pn}^{(\mathcal{P}'_{r_1})} T_{pn}^{(\mathcal{P}''_{r_2})} = \Upsilon^{(\mathcal{P}'_{r_1})} \Gamma^{(\mathcal{P}'_{r_1})} \Gamma^{(\mathcal{P}''_{r_2})} \Upsilon^{(\mathcal{P}''_{r_2})}. \tag{36}$$

The following equations hold for vertical polarization. Similar expressions can be found for the horizontally polarized case. The reflection coefficient $\Gamma^{(\cdot)}$ in (36), associated with a particular partial path, is given by [40]

$$\Gamma^{(\cdot)} = \begin{cases} \dfrac{\cos\theta_{i,pn}^{(\cdot)} - \sqrt{\epsilon_r}\cos\theta_{t,pn}^{(\cdot)}}{\cos\theta_{i,pn}^{(\cdot)} + \sqrt{\epsilon_r}\cos\theta_{t,pn}^{(\cdot)}}, & \text{for multipath via interior wall} \\ 1, & \text{otherwise.} \end{cases} \tag{37}$$

Further, $\Upsilon^{(\cdot)}$ in (36) is the total transmission coefficient for a wave traveling through the front wall. The refraction on the first and second interface, respectively, and k reverberations within the wall are considered [40]

$$\Upsilon^{(\cdot)} = \frac{2\cos\theta_{i,pn}^{(\cdot)}}{\cos\theta_{i,pn}^{(\cdot)} + \sqrt{\epsilon_r}\cos\theta_{t,pn}^{(\cdot)}} \frac{2\sqrt{\epsilon_r}\cos\theta_{t,pn}^{(\cdot)}}{\cos\theta_{i,pn}^{(\cdot)} + \sqrt{\epsilon_r}\cos\theta_{t,pn}^{(\cdot)}} \left(\frac{-\cos\theta_{i,pn}^{(\cdot)} + \sqrt{\epsilon_r}\cos\theta_{t,pn}^{(\cdot)}}{\cos\theta_{i,pn}^{(\cdot)} + \sqrt{\epsilon_r}\cos\theta_{t,pn}^{(\cdot)}} \right)^{2k}. \tag{38}$$

In both of the equations (37) and (38), $\theta_{i,pn}^{(\cdot)}$ and $\theta_{t,pn}^{(\cdot)}$ are the incident (in air) and refracted (in the medium) angles of the wave and ϵ_r is the relative permittivity of the interior wall. In the case of wall ringing multipath, k is larger then zero, otherwise it is zero. A more detailed derivation of the path loss coefficients can be found in [5].

APPENDIX B

JUSTIFICATION OF THE INVARIANCE OF COMPLEX AMPLITUDE ACROSS THE ARRAY

In the derivation of the multipath exploitation scheme, we assume that the complex path weights are invariant across the array elements and, therefore, can be replaced by a common weight. This approximation generally holds for far-field conditions, where all angles are approximately equal across all target/array element pairs. The

approximation also holds to a certain extent for the near-field case. To demonstrate this property, we examined the error for the near-field imaging with vertical polarization assumed throughout this work. We use an array length of 1.5 m and the imaged region is within a 4 m by 5 m room, whose center is at 4.5 m downrange. For the entire image grid, we calculate the individual path loss coefficients associated with a propagation path $\mathcal{P}_r$, according to (36). Subsequently, we calculate the relative errors, that arise when replacing the individual coefficients by a common amplitude factor $T_p^{(\mathcal{P}_r)}$, which is chosen as the mean. We assume a relative error threshold of 10% as acceptable and determine the number of $T_{pn}^{(\mathcal{P}_r)}$ meeting this criterion.

For the multipath associated with the back wall and the back right corner, the error of using $T_p^{(\mathcal{P}_r)}$ instead of $T_{pn}^{(\mathcal{P}_r)}$ is sufficiently low for all cases. Hence, large errors will not be encountered when using the above assumption. However, the approximation is less accurate when considering the multipath via the left side wall. For these paths, due to the higher variation in incident and reflection angles, we have a sufficiently low error for 90% of all possible target/array element pairs. This approximation error is still comparably low and will probably not affect the performance of the multipath exploitation scheme in near-field scenarios. Note that the reflection coefficients are purely real for perfect dielectric slabs. This alleviates the problem further, as the beamformer is less susceptible to amplitude errors as compared to phase errors.

REFERENCES

[1] F. Ahmad and M. Amin, "Multi-location wideband synthetic aperture imaging for urban sensing applications," *Journal of the Franklin Institute*, vol. 345, no. 6, pp. 618 – 639, September 2008.

[2] E. Baranoski, "Through-wall imaging: Historical perspective and future directions," *J. Franklin Institute*, vol. 345, no. 6, pp. 556 – 569, Sep. 2008.

[3] Y.-S. Yoon and M. Amin, "High-resolution through-the-wall radar imaging using beamspace MUSIC," *IEEE Transactions on Antennas and Propagation*, vol. 56, no. 6, pp. 1763 –1774, June 2008.

[4] M. Amin, Ed., *Through-the-Wall Radar Imaging*. CRC Press, 2010.

[5] P. Setlur, M. Amin, and F. Ahmad, "Multipath model and exploitation in through-the-wall and urban radar sensing," *IEEE Trans. Geosci. Remote Sens.*, vol. 49, no. 10, pp. 4021–4034, Oct. 2011.

[6] Y.-S. Yoon and M. Amin, "Spatial filtering for wall-clutter mitigation in through-the-wall radar imaging," *IEEE Transactions on Geoscience and Remote Sensing*, vol. 47, no. 9, pp. 3192 –3208, Sept. 2009.

[7] F. H. C. Tivive, M. G. Amin, and A. Bouzerdoum, "Wall clutter mitigation based on eigen-analysis in through-the-wall radar imaging," in *Proc. 17th Int. Conf. on Digital Signal Processing (DSP)*, Corfu, Greece, July 2011, pp. 1–8.

[8] M. Dehmollaian and K. Sarabandi, "Refocusing through building walls using synthetic aperture radar," *IEEE Transactions on Geoscience and Remote Sensing*, vol. 46, no. 6, pp. 1589–1599, 2008.

[9] F. H. C. Tivive, A. Bouzerdoum, and M. G. Amin, "An SVD-based approach for mitigating wall reflections in through-the-wall radar imaging," in *IEEE Radar Conference (RADAR)*, Kansas City, USA, May 2011, pp. 519–524.

[10] Y.-S. Yoon and M. Amin, "Compressed sensing technique for high-resolution radar imaging," in *Proceedings of SPIE Signal Processing, Sensor Fusion, and Target Recognition XVII*, vol. 6968, no. 1, Orlando, USA, March 2008, p. 69681A.

[11] F. Ahmad and M. G. Amin, "Through-the-wall human motion indication using sparsity-driven change detection," *IEEE Transactions on Geoscience and Remote Sensing*, vol. 51, no. 2, pp. 881 –890, February 2013.

[12] M. Leigsnering, C. Debes, and A. Zoubir, "Compressive sensing in through-the-wall radar imaging," in *IEEE International Conference on Acoustics, Speech and Signal Processing (ICASSP)*, Prague, Czech Republic, May 2011.

[13] R. Burkholder, "Electromagnetic models for exploiting multi-path propagation in through-wall radar imaging," in *Int. Conf. on Electromagnetics in Advanced Applications*, Torino, Italy, Sep. 2009, pp. 572 –575.

[14] T. Dogaru and C. Le, "SAR images of rooms and buildings based on FDTD computer models," *IEEE Trans. Geosci. Remote Sens.*, vol. 47, no. 5, pp. 1388 –1401, May 2009.

[15] S. Kidera, T. Sakamoto, and T. Sato, "Extended imaging algorithm based on aperture synthesis with double-scattered waves for UWB radars," *IEEE Trans. Geosci. Remote Sens.*, vol. 49, no. 12, pp. 5128 – 5139, Dec. 2011.

[16] E. L. Targarona, M. G. Amin, F. Ahmad, and M. Nájar, "Compressive sensing for through wall radar imaging of stationary scenes using arbitrary data measurements," in *Proc. 11th Intl. conf. on information science, signal processing, and their applications*, 2012.

[17] E. L. Targarona, M. G. Amin, F. Ahmad, and M. Nájar, "Wall mitigation techniques for indoor sensing within the cs framework," in *Proc. Seventh IEEE workshop on sensor array and multi-channel signal processing*, 2012.

[18] F. Ahmad and M. Amin, "Partially sparse reconstruction of behind-the-wall scenes," in *Proc. SPIE Symp. on Defense, Security, and Sensing, Compressive Sensing Conf.*, vol. 8365, Baltimore, USA, April 2012.

[19] J. Tian, J. Sun, G. Wang, and Y. Lu, "Compressive sensing based SAR post-processing algorithm for suppressing multipath ghosts," in *International Workshop on Compressed Sensing applied to Radar (CoSeRa 2012)*, 2012.

[20] W. Zhang, A. Hoorfar, C. Thajudeen, and F. Ahmad, "Full polarimetric beam-forming algorithm for through-the-wall radar imaging," *Radio Science*, vol. 46, pp. RS0E16–, Oct. 2011.

[21] F. Soldovieri, F. Ahmad, and R. Solimene, "Validation of microwave tomographic inverse scattering approach via through-the-wall experiments in semicontrolled conditions," *IEEE Geoscience and Remote Sensing Letters*, vol. 8, no. 1, pp. 123 –127, jan. 2011.

[22] F. Ahmad, M. Amin, and G. Mandapati, "Autofocusing of through-the-wall radar imagery under unknown wall characteristics," *IEEE Transactions on Image Processing*, vol. 16, no. 7, pp. 1785 –1795, july 2007.

[23] C. Thajudeen, A. Hoorfar, and W. Zhang, "Estimation of frequency-dependent parameters of unknown walls for enhanced through-the-wall imaging," in *IEEE International Symposium on Antennas and Propagation (APSURSI)*, july 2011, pp. 3070 –3073.

[24] F. Ahmad, M. Amin, and S. Kassam, "A beamforming approach to stepped-frequency synthetic aperture through-the-wall radar imaging," in *Proc. IEEE First International Workshop on Computational Advances in Multi-Sensor Adaptive Processing*, Puerto Vallarta, Mexico, December 2005.

[25] A. Karousos, G. Koutitas, and C. Tzaras, "Transmission and reflection coefficients in time-domain for a dielectric slab for UWB signals," in *IEEE Vehicular Technology Conference*, Singapore, May 2008, pp. 455–458.

[26] M. Amin, F. Ahmad, and W. Zhang, "A compressive sensing approach to moving target indication for urban sensing," in *IEEE Radar Conference (RADAR)*, Kansas City, USA, May 2011, pp. 509 –512.

[27] A. Gurbuz, J. McClellan, and W. Scott, "Compressive sensing for subsurface imaging using ground penetrating radar," *Signal Processing*, vol. 89, no. 10, pp. 1959 – 1972, October 2009.

[28] A. Gurbuz, J. McClellan, and W. Scott, "A compressive sensing data acquisition and imaging method for stepped frequency GPRs," *IEEE Transactions on Signal Processing*, vol. 57, no. 7, pp. 2640 –2650, July 2009.

[29] W. Zhang, M. G. Amin, F. Ahmad, A. Hoorfar, and G. E. Smith, "Ultrawideband impulse radar through-the-wall imaging with compressive sensing," *International Journal of Antennas and Propagation*, vol. 2012, p. 11, 2012.

[30] S. Wright, R. Nowak, and M. Figueiredo, "Sparse reconstruction by separable approximation," *IEEE Transactions on Signal Processing*, vol. 57, no. 7, pp. 2479–2493, July 2009.

[31] W. Deng, W. Yin, and Y. Zhang, "Group sparse optimization by alternating direction method," Department of Computational and Applied Mathematics, Rice University, Technical Report TR11-06, 2011.

[32] M. Yuan and Y. Lin, "Model selection and estimation in regression with grouped variables," *Journal of the Royal Statistical Society, Series B*, vol. 68, no. 1, pp. 49–67, December 2006.

[33] R. Baraniuk, V. Cevher, M. Duarte, and C. Hegde, "Model-based compressive sensing," *IEEE Transactions on Information Theory*, vol. 56, pp. 1982–2001, April 2010.

[34] Y. Eldar, P. Kuppinger, and H. Bolcskei, "Block-sparse signals: Uncertainty relations and efficient recovery," *IEEE Transactions on Signal Processing*, vol. 58, no. 6, pp. 3042 –3054, June 2010.

[35] J. Moulton, S. Kassam, F. Ahmad, M. Amin, and K. Yemelyanov, "Target and change detection in synthetic aperture radar sensing of urban structures," in *IEEE Radar Conference (RADAR)*, Rome, Italy, May 2008.

[36] M. G. Amin and F. Ahmad, "Change detection analysis of humans moving behind walls," *IEEE Transactions on Aerospace and Electronic Systems*, in press.

[37] M. Tuncer and A. Gurbuz, "Ground reflection removal in compressive sensing ground penetrating radars," *IEEE Geoscience and Remote Sensing Letters*, vol. 9, no. 1, pp. 23 –27, jan. 2012.

[38] C. Thajudeen, A. Hoorfar, F. Ahmad, and T. Dogaru, "Measured complex permittivity of walls with different hydration levels and the effect on power estimation of TWRI target returns," *Progress in Electromagnetic Research B*, vol. 30, pp. 177–199, 2011.

[39] D. Donoho, M. Elad, and V. Temlyakov, "Stable recovery of sparse overcomplete representations in the presence of noise," *Information Theory, IEEE Transactions on*, vol. 52, no. 1, pp. 6 – 18, jan. 2006.

[40] C. Balanis, *Advanced Engineering Electromagnetics*.   Wiley, 1989.

Michael Leigsnering (S'11) received the Dipl.-Ing. degree in electrical engineering and information technology from the Technische Universität Darmstadt in 2010. He is currently working towards his Ph.D. degree in the Signal Processing Group, Institute of Telecommunications, Technische Universität Darmstadt. His research interest lies in array signal processing with focus on through-the-wall radar imaging, compressive sensing, and multipath phenomena. He has been a visitor at Center for Advanced Communications, Villanova University, Villanova, PA in 2012 and 2013.

Fauzia Ahmad (S'97 – M'97 – SM'06) received her M.S. degree in electrical engineering in 1996 and Ph.D. degree in electrical engineering in 1997, both from the University of Pennsylvania, Philadelphia. From 1998 to 2000, she was an assistant professor in the College of Electrical and Mechanical Engineering, National University of Sciences and Technology, Pakistan. During 2000 to 2001, she served as an assistant professor at Fizaia College of Information Technology, Pakistan. Since 2002, she has been with the Center for Advanced Communications, Villanova University, where she is now a research associate professor and the Director of the Radar Imaging Lab. Dr. Ahmad has over 120 journal and conference publications in the areas of radar imaging, radar signal processing, waveform design and diversity, compressive sensing, array signal processing, sensor networks, ultrasound imaging, and over-the-horizon radar.
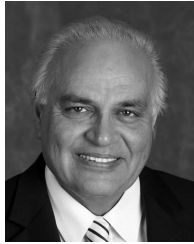
Moeness G. Amin (F'01) received his Ph.D. degree in 1984 from University of Colorado, in electrical engineering. He has been a member of the faculty of the Department of Electrical and Computer Engineering at Villanova University since 1985. In 2002, he became the Director of the Center for Advanced Communications, College of Engineering. Dr. Amin is the recipient of the 2009 Individual Technical Achievement Award from the European Association of Signal Processing, and the recipient of the 2010 NATO Scientific Achievement Award. He is a Fellow of the International Society of Optical Engineering, and a Fellow of the Institute of Engineering and Technology (IET). He is a recipient of the IEEE Third Millennium Medal, recipient of the Chief of Naval Research Challenge Award, 2010, Distinguished Lecturer of the IEEE Signal Processing Society, 2003 to 2004, active member of the Franklin Institute Committee on Science and the Arts, recipient of Villanova University Outstanding Faculty Research Award, 1997, and the recipient of the IEEE Philadelphia Section Award, 1997. He is a member of SPIE, EURASIP, ION, Eta Kappa Nu, Sigma Xi, and Phi Kappa Phi.

He has over 500 journal and conference publications in the areas of wireless communications, time-frequency analysis, smart antennas, waveform design and diversity, interference cancellation in broadband communication platforms, anti-jam GPS, target localization and tracking, direction finding, channel diversity and equalization, ultrasound imaging and radar signal processing. He is a recipient of seven best paper awards. Dr. Amin currently serves on the Overview Board of the IEEE Transactions on Signal Processing. He also serves on the Editorial Board of the EURASIP Journal on Advances in Signal Processing and the Editorial Board of the Signal Processing Magazine. He was a plenary speaker at ICASSP 2010. Dr. Amin was the Special Session Cochair of the 2008 IEEE International Conference on Acoustics, Speech, and Signal Processing. He was the Technical Program Chair of the 2nd IEEE International Symposium on Signal Processing and Information Technology, 2002. Dr. Amin was the General and Organization Chair of the IEEE Workshop on Statistical Signal and Array Processing, 2000. He was the General and Organization Chair of the IEEE International Symposium on Time-Frequency and Time-Scale Analysis, 1994. He was an Associate Editor of the IEEE Transactions on Signal Processing during 1996–1998. He was a member of the IEEE Signal Processing Society Technical Committee on Signal Processing for Communications during 1998–2002. He was a member of the IEEE Signal Processing Society Technical Committee on Statistical Signal and Array Processing during 1995–1997. Dr. Amin was the Guest Editor of the Journal of Franklin Institute September 2008 Special Issue on Advances in Indoor Radar Imaging. He was a Guest Editor of the IEEE Transactions on Geoscience and Remote Sensing May 2009 Special Issue on Remote Sensing of Building Interior, and a Guest Editor of the IET Signal Processing December 2009 Special Issue on Time-Frequency Approach to Radar Detection, Imaging, and Classification.

Abdelhak M. Zoubir (F'08) received the Dr.-Ing. from Ruhr-Universität Bochum, Germany, in 1992. He was with Queensland University of Technology, Australia, from 1992 to 1998, where he was an Associate Professor. In 1999, he joined Curtin University of Technology, Australia, as a Professor of Telecommunications and was Interim Head of the School of Electrical and Computer Engineering from 2001 to 2003. In 2003, he moved to Technische Universität Darmstadt, Germany, as Professor of Signal Processing and Head of the Signal Processing Group. His research interest lies in statistical methods for signal processing with emphasis on bootstrap techniques, robust detection and estimation and array processing applied to telecommunications, radar, sonar, car engine monitoring, and biomedicine. He published more than 300 journal and conference papers on these areas.

Professor Zoubir was Technical Chair of the 11th IEEE Workshop on Statistical Signal Processing (SSP 2001), General Co-Chair of the 3rd IEEE International Symposium on Signal Processing and Information Technology (ISSPIT 2003), and of the 5th IEEE Workshop on Sensor Array and Multi-channel Signal Processing (SAM 2008). He is the General Co-Chair of EUSIPCO 2013 to be held in Marrakesh, Morocco, and Technical Co-Chair of ICASSP-14 to be held in Florence, Italy. He is an IEEE Distinguished Lecturer (Class 2010–2011). He was an Associate Editor of the IEEE Transactions On Signal Processing (1999–2005), a Member of the Senior Editorial Board of the IEEE Journal On Selected Topics In Signal Processing (2009–2011), and currently serves on the Editorial Boards of the European Association of Signal Processing (EURASIP) journals Signal Processing and the Journal on Advances in Signal Processing (JASP). He is the Editor-in-Chief of the IEEE Signal Processing Magazine (2012–2014). He is Past-Chair (2012) of the IEEE SPS Technical Committee Signal Processing Theory and Methods (SPTM) [Chair (2010–2011), Vice-Chair (2008–2009), and Member (2002–2007)], and a Member of the IEEE SPS Technical Committee Sensor Array and Multi-channel Signal Processing (SAM) (2007–2012). He also serves on the Board of Directors of the EURASIP.